

Code carrier divergence monitoring for dual-frequency GBAS

Yiping Jiang¹  · Carl Milner¹ · Christophe Macabiau¹

Received: 18 February 2016 / Accepted: 6 September 2016 / Published online: 28 September 2016
© Springer-Verlag Berlin Heidelberg 2016

Abstract The ground-based augmentation system (GBAS) includes a ground monitor designed to protect against a code carrier divergence (CCD) fault originating from the satellite payload. The current single-frequency GBAS solutions known as GBAS approach service types (GAST) C and D which support Category I and Category II/III precision approaches, respectively, both utilize this monitor, but it has been noted that the test metric is subject to non-Gaussian tails as a result of nominal ionospheric errors. It has been observed that the ionospheric delay seen at low elevations can trigger alarms which are not distinguishable from the payload fault and thus impact the continuity and availability of GAST-D. The future GAST-F concept is designed to meet Category II/III precision approach using multi-frequency measurements which allows the CCD monitor proposed to be free of ionospheric influence. In order to address the full threat space, the combination of three ionospheric-free statistics is needed to form the test metric. This test metric is characterized through a combination of empirical multi-frequency data analysis and theoretical derivations leading to an approximately diagonal covariance matrix consisting of standard deviations 0.0017, 0.0050 and 0.0046 m/s, compared to 0.00399 m/s for the current single-frequency GAST-D design. Results from extensive simulations assessing the monitor's integrity performance are then provided which

show superior performance to the existing design. The proposed GAST-F monitor detects a divergence less than half the size of the GAST-D one, with the same probability of missed detection. Under the GAST-F concept, the aircraft may be operating in ionospheric-free smoothing mode which leads to inflation of the divergence impacts for much of the threat space and degrades the performance of all potential CCD monitors. It is shown that a longer delay is required for the incorporation of a smoothed ranging measurement into the solution. The worst-case fault mode requires a delay of 132 s over the current value 50 s.

Keywords GBAS · Integrity monitor · Code carrier divergence

Introduction

Ground-based augmentation system (GBAS) is intended to support precision approach operations and is currently standardized at the International Civil Aviation Organization (ICAO) to support Category I with a 200 ft decision height for precision instrument approach and landing known as GBAS approach service types (GAST)-C. A single-frequency GPS-based GAST-D, intended to support Category III minima with lower than 100 ft decision height, is under development. However, the GAST-D solution while meeting the requirements most of the time at most locations can be susceptible to ionospheric activity and interference. With the forthcoming GNSS environment, GAST-F has been designated to the provision of CAT III services using multi-constellation and dual-frequency corrections which will mitigate the issues raised under GAST-D and is being investigated within the European SESAR program (WP 15.3.7). Furthermore, the

✉ Yiping Jiang
jiang@recherche.enac.fr

Carl Milner
milner@recherche.enac.fr

Christophe Macabiau
macabiau@recherche.enac.fr

¹ ENAC, Toulouse, France

enhanced performance of the navigation system could enable worse performing aircraft, those with larger flight technical errors (FTE), to meet the requirement. This conclusion is based on the fact that total system performance depends upon both the navigation system error (NSE) and the FTE (SARPs 2009).

In the design of GAST-F, one aspect which may be revisited to garner better performance is the design of integrity monitors for the array of threats which constitute a risk to GBAS. In addition, these threats may differ when considering new signals and constellations. Ground monitoring of the code carrier divergence (CCD) threat addresses the impact of a satellite payload fault, which results in the code and carrier of the broadcast signal to diverge excessively (Gleason and Gebre-Egziabher 2009). This threat should be distinguished from the acceleration threat, where the code and carrier accelerate in unison caused by a satellite clock failure. A specific monitor is assigned for the acceleration threat, which is the excessive acceleration monitor (Stakkeland et al. 2014). For the CCD threat, the effect of multiple monitors was evaluated (Brenner and Liu 2010) including the CCD rate monitor (Simili and Pervan 2006), the excessive acceleration monitor (Stakkeland et al. 2014) and the carrier rate monitor (Tang et al. 2010) for GAST-D. In this study, only the CCD rate monitor is redesigned and evaluated for GAST-F. On detection of such failures, the satellite is flagged as faulty in the correction messages and excluded by the aircraft.

In the GAST-D CCD monitor, nominal ionosphere delay at low elevation angles leads to non-Gaussian tails of the test metrics, which is dealt with by inflating the standard deviation of the metric noise (Simili and Pervan 2006). Also, in case of large temporal ionospheric gradients, alarms are triggered as would for a payload CCD. However, while the ground CCD monitor may provide some protection against extreme gradients it is not intended to flag nominal ionospheric gradients which are partly mitigated in the correction process and do not represent an integrity threat. With multiple frequency measurements, it is possible to form observables in which the ionospheric delay is removed.

In GAST-D, the ground station and user smooth the measurements with the same Hatch filter (Hatch 1982). For the dual-frequency GBAS structure, there are two additional smoothing techniques under consideration: the divergence-free (DF) and the ionosphere-free (IF) (Hwang et al. 1999). The evaluation of possible processing modes for GAST-F is ongoing, which needs both to be backward compatible with legacy GAST-C/D services and fit within the tight VHF data broadcast (VDB) capacity constraints (Milner et al. 2015). While a finalized solution is yet to be proposed within standardization fora, what may be

assumed is that a fully ionosphere-free solution, based on the ionosphere-free smoothing technique, will form one airborne mode. The CCD monitor must be able to detect divergences in any of the raw measurements that could be used to form the corrected smoothed ranges in the airborne subsystem.

First, the GBAS processing techniques are outlined including how the CCD impacts the system. Then, the current GAST-D CCD monitor is introduced followed by the proposed GAST-F CCD monitor. The statistical model of the new monitor is derived both theoretically and with empirical GPS data. Compliance to the requirement is then analyzed where the results of probability of missed detection (PMD) versus the differential error in different situations are shown.

Processing modes

In GBAS, both the ground and airborne subsystems smooth the raw pseudoranges with the same Hatch filter (Hatch 1982),

$$\bar{\rho}_g(t) = \alpha\rho(t) + (1 - \alpha)[\hat{\rho}(t - T) + \varphi(t) - \varphi(t - T)] \quad (1)$$

where $\bar{\rho}_g$ is the ground-smoothed pseudorange, ρ is the raw code measurement, φ is the raw phase measurement, $\alpha = \frac{T}{\tau}$ is the filter weight with τ as the time constant and T as the sample interval. The same definition can be applied to $\bar{\rho}_a$, the airborne carrier-smoothed pseudorange. The filter may have a variant time constant increasing with the time since initialization up to a maximum value of 30 s for GAST-D and 100 s for GAST-C or invariant and fixed at this value. The output of the Hatch filter may be expressed using the approximate continuous Laplace form as follows:

$$\bar{\Psi} = F\Psi + (1 - F)\Phi \quad (2)$$

where $F(s) = \frac{1}{\tau s + 1}$ and the inputs ρ and φ have been generalized as Ψ and Φ (refer to Table 1).

Besides monitoring the GNSS signals, the GBAS ground station transmits differential corrections via the VDB subsystem every 0.5 s to mitigate spatially and temporally correlated errors. Among the broadcast corrections, PRC is the pseudorange correction (ED-114A) and RRC is the rate of change of PRC based on the current and immediately prior corrections, defined as follows

$$\text{PRC}_{\text{csc}} = r - \bar{\rho}_g - c\Delta t_{\text{sv},t_e} \quad (3)$$

$$\text{PRC}_{\text{sca}}(i,j) = \text{PRC}_{\text{csc}}(i,j) - \sum_{i=1}^N w_i \text{PRC}_{\text{csc}}(i,j) \quad (4)$$

$$\text{PRC}(i) = \frac{1}{M} \sum_{j=1}^M \text{PRC}_{\text{sca}}(i,j) \quad (5)$$

Table 1 GAST-F data processing candidates

	Ψ	Φ	Note
SF1	ρ_1	φ_1	L1/E1 frequency $f_{L1} = 1575.42$ MHz,
SF5	ρ_5	φ_5	L5/E5a frequency $f_{L5} = 1176.45$ MHz,
DF1	ρ_1	$\frac{\gamma+1}{\gamma-1}\varphi_1 - \frac{2}{\gamma-1}\varphi_5$	$\gamma = \frac{f_{L1}^2}{f_{L5}^2} \approx 1.79, \frac{\gamma+1}{\gamma-1} \approx 3.53$
DF5	ρ_5	$\frac{2\gamma}{\gamma-1}\varphi_1 - \frac{\gamma+1}{\gamma-1}\varphi_5$	$\frac{1}{\gamma-1} \approx 1.26, \frac{\gamma}{\gamma-1} \approx 2.26$
IF	$\frac{\gamma}{\gamma-1}\rho_1 - \frac{1}{\gamma-1}\rho_5$	$\frac{\gamma}{\gamma-1}\varphi_1 - \frac{1}{\gamma-1}\varphi_5$	

where PRC_{csc} is the carrier-smoothed pseudorange correction, r is the geometric range computed based on ground station coordinates, c is the speed of light, Δt_{sv} is the satellite clock correction from the navigation message, PRC_{sca} is the ground carrier-smoothed and receiver clock-adjusted correction, i and j indicate satellite and ground receiver, w_i is the weighting factor whose value can be chosen as $\theta_i / \sum_{i=1}^N \theta_i$ for N satellites tracked at elevation angle θ_i and M is the number of ground receivers. After applying corrections, the differential pseudorange ρ_c is computed as,

$$\rho_c = \bar{\rho}_a + PRC + RRC(t_a - t_g) + TC + \Delta t_{sv} \tag{6}$$

where t_a is the time of the airborne measurement and of the application of PRC, t_g is the ground correction measurement time, TC is the tropospheric correction and Δt_{sv} is the satellite clock correction in meters (ED-114A) applied at t_a .

The data processing is shown in Fig. 1 which includes both smoothing and correction modules. The filter inputs Ψ and Φ depend upon the choice of smoothing technique whose candidates for GAST-F are listed in Table 1. Five candidates are considered: SF1 (GAST-D) the single-frequency smoothing of the L1C/A code measurement ρ_1 with the L1 phase measurement φ_1 ; SF5 the single-frequency smoothing on L5 and E5a code measurement ρ_5 with phase measurement φ_5 ; DF1 the divergence-free smoothing of ρ_1 with a combination of φ_1 and φ_5 ; DF5 the divergence-free smoothing of ρ_5 with a combination of φ_1 and φ_5 ; and IF the ionospheric-free smoothing (Hwang et al. 1999). The time constant τ may be 30 s, 100 s or potentially larger.

DF1 and DF5 are candidates that remove the extra ionospheric divergence caused by the smoothing filter in single-frequency data processing, but the ionospheric delay at the current epoch remains. Since they are formed of only a single-code measurement, if carrier phase noise and multipath are reasonably neglected, the same noise properties as the single-frequency counterpart are maintained. IF is able to remove all ionosphere delay but results in an inflated standard deviation of the code multipath and noise, mainly caused by the inflation factor 2.26 for ρ_1 in Table 1.

For the SF1 mode, denoting a divergence on ρ_1 as $d_{\rho 1}$ and on φ_1 as $d_{\varphi 1}$, the steady states are derived as follows,

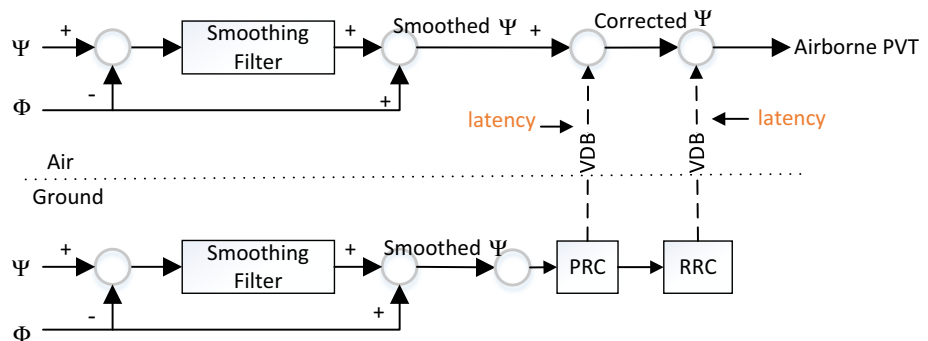
$$\lim_{s \rightarrow 0} sE(\bar{\Psi}_{SF1}) = \lim_{s \rightarrow 0} s \left[F \frac{d_{\rho 1}}{s^2} + (1 - F) \frac{d_{\varphi 1}}{s^2} \right] = \lim_{s \rightarrow 0} \left(\frac{s}{\tau s + 1} \cdot \frac{d_{\rho 1}}{s^2} + \frac{\tau s^2}{\tau s + 1} \cdot \frac{d_{\varphi 1}}{s^2} \right) \tag{7}$$

$$\lim_{s \rightarrow 0} s [sE(\bar{\Psi}_{SF1}) - E(\bar{\Psi}_{SF1,0})] = \lim_{s \rightarrow 0} \left(\frac{s^2}{\tau s + 1} \cdot \frac{d_{\rho 1}}{s^2} + \frac{\tau s^3}{\tau s + 1} \cdot \frac{d_{\varphi 1}}{s^2} \right) = d_{\rho 1} \tag{8}$$

where $E()$ is the notation for mean, $\bar{\Psi}_{SF1}$ is the filter output in (2) with SF1 mode and $\bar{\Psi}_{SF1,0}$ is the initial state of $\bar{\Psi}_{SF1}$. It is concluded that a steady state of the smoothed range error in (2) is $d_{\rho 1} \tau$ when $d_{\rho 1} = 0$ as shown in (7). Also, the rate of the mean smoothed range error has steady-state value $d_{\rho 1}$ in (8). Similar steady-state results for the other data processing modes in Table 1 can be derived.

However, the filters are not ensured to be in steady states since a fault may occur at any time. The requirement on the

Fig. 1 GBAS data processing mechanism



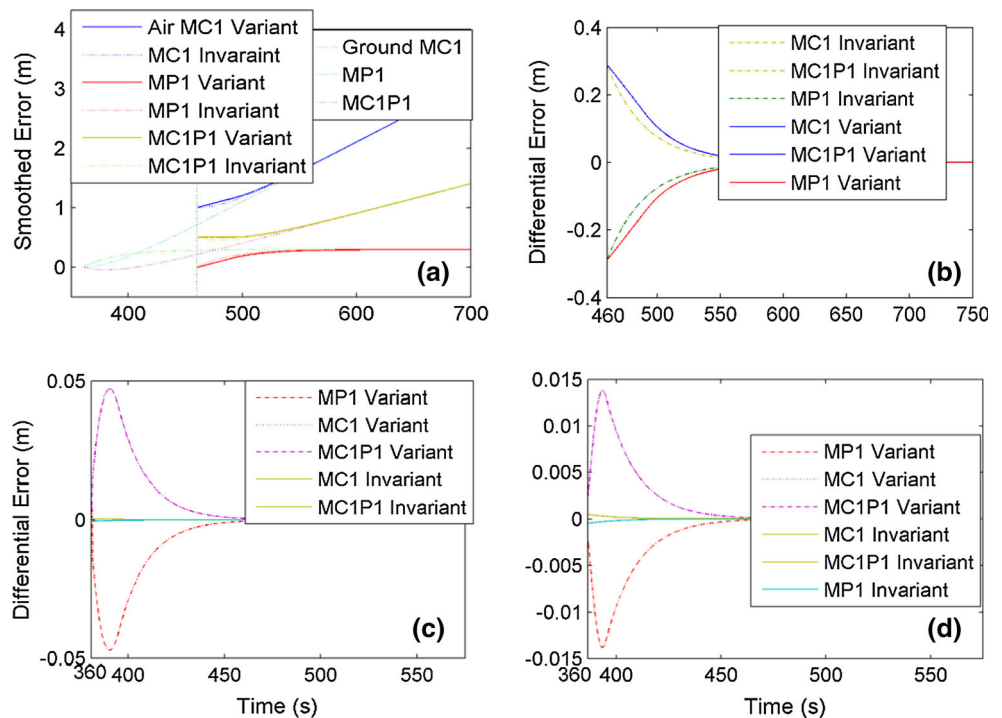
ground subsystem is defined in the form of “the probability of an error $|E_R|$, which is greater than a certain size for the corrected pseudorange ρ_c and caused by a ranging source failure due to signal deformation, CCD, excessive acceleration and ephemeris error and which is not detected and reflected in the broadcast message within the required time to alert, shall be less than a required small probability in any one landing when multiplied by a prior probability” (SARPs 2009). Therefore, the differential bias E_R due to the CCD failure is of interest, which is a function of the following parameters: $\{\tau, t_g, t_a, t_f, t_{g,0}, t_{a,0}, t_{\text{delay}}, d\}$, where t_g is the ground correction measurement time, t_a is the airborne measurement time at which E_R is determined, t_f is the fault onset time, $t_{g,0}$ the ground filter initialization time, $t_{a,0}$ is the airborne filter initializing time, t_{delay} is the time delay from initialization of the airborne filter to incorporation in the solution and $d = [d_{\rho 1}, d_{\varphi 1}, d_{\rho 5}, d_{\varphi 5}]$ is the divergence magnitude vector with $d_{\rho 5}, d_{\varphi 5}$ being the divergence on ρ_5 and φ_5 , respectively. The following conditions define the satellite clock failure: $d_{\rho 1} = d_{\varphi 1}$, $d_{\rho 5} = d_{\varphi 5}$, $\frac{d_{\rho 1}}{d_{\rho 5}} = \frac{f_{L5}}{f_{L1}}$. The case of $d_{\rho 1} = -d_{\varphi 1}$, $d_{\rho 5} = -d_{\varphi 5}$, $\frac{d_{\rho 1}}{d_{\rho 5}} = \frac{1}{\gamma}$ characterizes ionospheric divergence.

CCD has 15 fault modes in GAST-F including 4 single-divergence fault modes: Code L1 (MC1), Code L5 (MC5), Carrier L1 (MP1) and Carrier L5 (MP5), 6 dual-divergence fault modes with Code L1+Code L5 (MC15), Code L1+Carrier L1 (MC1P1), etc., 4 triple-divergence fault modes such as Code L1+Carrier L1+Carrier L5

(MC1P15) and 1 quad-divergence fault mode with Code L1+Code L5+Carrier L1+Carrier L5 (MC15P15).

Figure 2 is used to illustrate the transient states of the smoothing error and the differential error with simulated GAST-D data processing, where the measurement is a constant value plus the divergence d in the simulation. Since the aircraft can start tracking a satellite tracked by the ground at any time, the ground filter is assumed to start at $t_{g,0} = 0$ s, and the results are shown by varying the relative start time of the aircraft filter start and fault. Panel (a) shows the smoothing error where the aircraft filter initializes after the fault onset for the ground filter and the variant and invariant forms of the airborne filter. The result is shown from the fault onset time $t_f = 360$ s, and the airborne filter results start from $t_{a,0} = 460$ s. The following three fault modes are used: MC1, $d = [0.01, 0, 0, 0]$ m/s; MP1, $d = [0, 0.01, 0, 0]$ m/s; and MC1P1, $d = [0.005, -0.005, 0, 0]$ m/s. Panel (b) shows the differential error E_R from the airborne initialization time $t_{a,0} = 460$ s with the same settings as in (a), where slightly larger transient response is observed in the case of the variant filter. Panel (c) shows E_R when $t_{a,0} = t_f = 360$ s and Panel (d) refers to the case when $t_f = 460$ s and $t_{a,0} = 360$ s. The largest value of E_R is observed in (b). Therefore, the worst-case differential error occurs when the airborne filter begins after the fault onset time, assuming the ground filter has converged to the faulty steady state, without considering the delay to incorporation into solution. The effect of integrity monitors for detection of the divergence is not considered here.

Fig. 2 GAST-D 30 s data processing error with an example divergence. **a** Smoothed error with $t_{a,0} > t_f$; **b** Differential error E_R with $t_{a,0} > t_f$; **c** E_R with $t_{a,0} = t_f$; **d** E_R with $t_{a,0} < t_f$



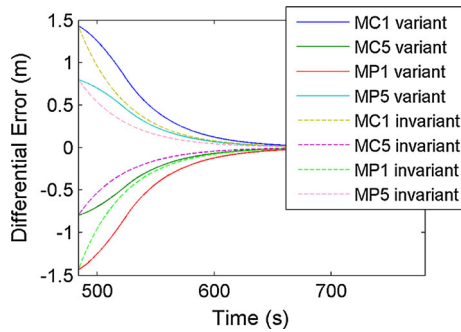


Fig. 3 IF 100 s E_R with single-divergence fault modes and $t_{a,0} > t_f$

Similarly, Fig. 3 shows the results of IF 100 s with $t_{a,0} = 460$ s, $t_f = 360$ s for the fault modes MC1, $d = [0.01, 0, 0, 0]$ m/s; MP1, $d = [0, 0.01, 0, 0]$ m/s; MC5, $d = [0, 0, 0.01, 0]$ m/s; and MP5, $d = [0, 0, 0, 0.01]$ m/s. Significantly larger values of the differential error are observed as a result of the inflation factors 2.26 and 1.26 on L1 and L5 separately for both code and carrier in Table 1. It is concluded that if the aircraft computes its position using IF observables, then this places a greater burden on the CCD monitor. The steady state is achieved around 108 s after filter initialization with the 30 s time constant shown in Fig. 2 and 360 s with the 100 s time constant shown in Fig. 3.

GAST-D CCD monitor

There are five threats characterized in GAST-D which must be mitigated including the ionospheric anomaly threat, CCD threat, ephemeris failure threat, acceleration threat and signal deformation threat, among which the extension of the CCD threat for GAST-F is of concern here. Only the ground monitor is of concern here, with the airborne CCD monitor addressing ionospheric threats. The existing GAST-D single-frequency CCD monitor utilizes the single-frequency code minus carrier combination (CMC),

$$\chi_1 = \rho_1 - \varphi_1 \tag{9}$$

where common errors to code and carrier measurements are removed, such as satellite and receiver clock offsets and tropospheric delay.

The rate of change is the difference between current epoch k and immediate prior epoch $k-1$, removing constant errors, e.g. the integer ambiguity, the inter system biases, the inter frequency biases and the group delay. The latter three are caused by hardware differences over the signal paths of the satellite transmitter depending on both frequency and code. Moreover, slowly varying biases in the code minus carrier are largely removed. The leftover errors appear in the form of the rate of change of the ionospheric delay, multipath and

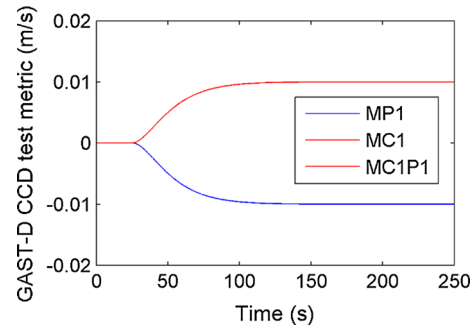


Fig. 4 Converging of the GAST-D test metric with divergence

noise with the phase multipath rate and noise rate being negligible. The discrete rate of change of χ_1 is $\dot{\chi}_1$,

$$\dot{\chi}_1(k) = \frac{\chi_1(k) - \chi_1(k-1)}{T} = 2\dot{I}_1(k) + \dot{\eta}_{\rho_1}(k) \tag{10}$$

where \dot{I}_1 is the rate of change of L1/E1 ionosphere delay and $\dot{\eta}_{\rho_1}$ is the rate of change of L1/E1 code multipath and noise. Two cascaded first-order low-pass filters are used in the GAST-D CCD monitor with Laplace representation,

$$F_m = \frac{1}{(\tau_m s + 1)^2} \tag{11}$$

where τ_m is the time constant for CCD monitor. Shorter time constants lead to faster detection of a CCD failure and the system is less susceptible to the buildup of divergence-induced filter lag errors, but results in a noisier test metric. The test metrics of the GAST-D CCD monitor x and the steady state of its non-centrality parameter are,

$$x = F_m \dot{\chi}_1 = s F_m \chi_1 \tag{12}$$

$$\lim_{s \rightarrow 0} s F_m E(\dot{\chi}_1) = \frac{s^2}{(\tau_m s + 1)^2} \frac{d_1}{s^2} = d_1 \tag{13}$$

where the steady state $d_1 = d_{\rho_1} - d_{\varphi_1}$ is independent of the time constant. The fault space which the GAST-D CCD monitor can protect against is expressed as,

$$\text{Fault space } _D = \{d_{\rho_1} \neq d_{\varphi_1} | d_{\rho_1}, d_{\varphi_1} \in \mathbb{R}\} \tag{14}$$

The case $d_{\rho_1} = d_{\varphi_1}$ defines a satellite clock failure, which is to be detected by the excessive acceleration monitor since the GAST-D CCD monitor provides no protection against this threat.

The GAST-D monitor standard deviation, σ_x , is characterized as 0.00399 m/s which incorporates an inflation factor to account for the non-Gaussian ionospheric error. The probability of false alarm (PFA) allocated for the CCD monitor is 10^{-7} per 15 s which leads to a detection threshold of 0.0233 m/s (Simili and Pervan 2006). Figure 4 simulates the response of the GAST-D CCD monitor for fault modes MC1, $d = [0.01, 0, 0, 0]$ m/s; MP1, $d = [0,$

0.01, 0, 0] m/s; and MC1P1, $d = [0.005, -0.005, 0, 0]$ m/s. The input measurement is a constant value plus the divergence d , and the output is the test metric x .

Proposed GAST-F CCD monitor

To our knowledge, the CCD payload fault has never been observed during real operations. In order to maintain conservatism, the most general form is assumed in this GAST-F CCD analysis. It may be possible to limit the threat space in the future which would allow the monitor design to be re-examined. The GAST-F CCD monitor needs to protect the aircraft against code and carrier phase divergences on both frequencies. Furthermore, as noted in the introduction, it is preferable that the monitor be insensitive to the ionosphere delay so to avoid false detections of payload faults under high ionospheric activity. There are several ionosphere-free combinations of interest, defined as follows: χ_{C1} is the CMC on L1 with the ionosphere delay removed by carrier phase combination; χ_{C2} is the CMC on L5 with the ionosphere delay removed by carrier phase combination; χ_{C3} is the IF combination on code measurements and χ_{C4} is the IF combination on phase measurements; χ_{C5} is the IF combination on CMC, which is a linear combination of χ_{C1} and χ_{C2} with $\chi_{C5} = \frac{\gamma}{\gamma-1}\chi_{C1} - \frac{1}{\gamma-1}\chi_{C2}$. The first four combinations are,

$$\begin{aligned} \chi_{C1} &= \rho_1 - \varphi_1 - \frac{2}{\gamma-1}(\varphi_1 - \varphi_5) \\ &= \rho_1 - \frac{\gamma+1}{\gamma-1}\varphi_1 + \frac{2}{\gamma-1}\varphi_5 \end{aligned} \tag{15}$$

$$\begin{aligned} \chi_{C2} &= \rho_5 - \varphi_5 - \frac{2\gamma}{\gamma-1}(\varphi_1 - \varphi_5) \\ &= \rho_5 - \frac{2\gamma}{\gamma-1}\varphi_1 + \frac{\gamma+1}{\gamma-1}\varphi_5 \end{aligned} \tag{16}$$

$$\chi_{C3} = \frac{\gamma}{\gamma-1}\rho_1 - \frac{1}{\gamma-1}\rho_5 \tag{17}$$

$$\chi_{C4} = \frac{\gamma}{\gamma-1}\varphi_1 - \frac{1}{\gamma-1}\varphi_5 \tag{18}$$

Two sets of combinations can be used to design the new monitor to cover the full threat space: $\{\chi_{C1}, \chi_{C2}, \chi_{C3}\}$ and $\{\chi_{C1}, \chi_{C2}, \chi_{C4}\}$.

After differencing between two adjacent epochs to compute the rate, the rate of χ_{C1} and χ_{C2} are geometry free with only multipath and noise errors remaining, while the rate of χ_{C3} needs compensation of the satellite motion, receiver and satellite clock, and troposphere. $\dot{\chi}_{C1}$ is defined as the rate of change of χ_{C1} between current and immediate prior epochs,

$$\dot{\chi}_{C1}(k) = \frac{\chi_{C1}(k) - \chi_{C1}(k-1)}{T} = \dot{\eta}_{\rho 1}(k) \tag{19}$$

The difference between two epochs removes biases that change little between epochs. The residual error is the multipath and noise rate on code L1 measurements $\dot{\eta}_{\rho 1}$. Similarly, the rate of χ_{C3} is $\dot{\chi}_{C3}$,

$$\begin{aligned} \dot{\chi}_{C3}(k) &= \frac{\chi_{C3}(k) - \chi_{C3}(k-1)}{T} \\ &= \dot{r}(k) + ci_{rx}(k) - ci_{sv}(k) + \dot{J}(k) + \frac{\gamma}{\gamma-1}\dot{\eta}_{\rho 1}(k) \\ &\quad - \frac{1}{\gamma-1}\dot{\eta}_{\rho 5}(k) \end{aligned} \tag{20}$$

Since $\dot{\chi}_{C3}$ is not geometry free, it is necessary to be compensated for satellite motion \dot{r} , receiver clock drift i_{rx} , satellite clock drift i_{sv} and the troposphere delay rate \dot{J} . $\dot{\eta}_{\rho 5}$ is the discrete rate of change of L5/E5a code multipath and noise. The receiver clock rate is estimated by averaging all the geometry-free satellites $\dot{\chi}_{C3,n}$,

$$ci_{rx} = \frac{1}{N-1} \sum_{h \neq i} (\dot{\chi}_{C3,h} - \dot{r}_h + ci_{sv,h} - \dot{J}) \tag{21}$$

where h indicates the satellites excluding the satellite i that is being tested and N is the total number of satellites. The satellite-based augmentation system (SBAS) troposphere model is used to estimate \dot{J} (DO-229D 2006). The compensated $\dot{\chi}_{C3}$ with the residual multipath and noise is noted as $\dot{\chi}_{C3_C}$ in (22),

$$\begin{aligned} \dot{\chi}_{C3_C} &= \dot{\chi}_{C3} - \dot{r} + ci_{sv} - ci_{rx} - \dot{J} \\ &= \frac{\gamma}{\gamma-1}\dot{\eta}_{\rho 1}(k) - \frac{1}{\gamma-1}\dot{\eta}_{\rho 5}(k) \end{aligned} \tag{22}$$

The compensated $\dot{\chi}_{C4}$ is denoted as $\dot{\chi}_{C4_C}$, which is derived in a similar manner. If $\dot{\chi}_{C4_C}$ is filtered, the influence of the satellite orbit and clock appears above the multipath noise. With the requirement of real-time monitoring, $\dot{\chi}_{C4_C}$ could be used directly without filtering. The statistics used to form the GAST-F test metrics are,

$$x_1 = F_m \dot{\chi}_{C1}, \quad x_2 = F_m \dot{\chi}_{C2}, \quad x_3 = F_m \dot{\chi}_{C3_C}, \quad x_4 = \dot{\chi}_{C4_C} \tag{23}$$

where F_m is the second-order filter in GAST-D. Defining vectors $X_u = [x_1, x_2, x_3]$ and $X_v = [x_1, x_2, x_4]$, the quadratic forms are proposed as the candidate dual-frequency test metrics,

$$x_u = X_u Q_u^{-1} X_u^T \sim \chi^2(3, \delta_u) \tag{24}$$

$$x_v = X_v Q_v^{-1} X_v^T \sim \chi^2(3, \delta_v) \tag{25}$$

where Q_u and Q_v are the covariance matrix of vector X_u and X_v respectively, and $\delta_{u(v)}$ is the non-centrality

parameter. Using Cholesky decomposition of Q_u and Q_v , the components of vector X_u and X_v are standardized and decorrelated, resulting in a Chi-squared metric with 3 degree of freedom assuming the noise is Gaussian (Kay 1998).

For GAST-F, the conservative assumption is that the divergence vector d may take any value in \mathbb{R}^4 . However, divergences which do not result in a differential error, such as those which appear like ionospheric divergences to an ionospheric-free user, do not require monitoring. Therefore, the GAST-F fault space is defined as,

$$\text{Fault space}_F = \left\{ d_{\rho 1} \neq -d_{\varphi 1} \cup d_{\rho 5} \neq -d_{\varphi 5} \cup \frac{d_{L5}}{d_{L1}} \neq \frac{f_{L1}^2}{f_{L5}^2} \right. \\ \left. | d = [d_{\rho 1}, d_{\varphi 1}, d_{\rho 5}, d_{\varphi 5}] \in \mathbb{R}^4 \right\} \tag{26}$$

Comparing the fault space of GAST-D in (14) and GAST-F in (26), the GAST-D CCD monitor does not raise an alarm for the satellite clock failure, while this is the case for the proposed GAST-F monitor. Therefore, the proposed GAST-F CCD monitor has a redundant part of fault space covered by the excessive acceleration monitor already. The proposed GAST-F monitor does not only detect CCD, but also provides some protection against steps and ramp errors due to other faults, except the ionospheric divergence. With the same PFA as in GAST-D, the threshold for the Chi-squared statistic is 40.96.

The steady state of the deterministic component of the test statistics before and after the GAST-D CCD filter remains the same as proved in (13). The same conclusion can be derived for x_1, x_2 and x_3 . When x_u is at steady state, its deterministic component d_x is,

$$d_x = \begin{bmatrix} d_{\rho 1} - 3.53d_{\varphi 1} + 2.53d_{\varphi 5} \\ d_{\rho 5} - 4.53d_{\varphi 1} + 3.53d_{\varphi 5} \\ 2.26d_{\rho 1} - 1.26d_{\rho 5} \end{bmatrix} \tag{27}$$

Therefore, the non-centrality parameter is $\delta_u = d_x^T Q_u^{-1} d_x$, which is used later for deriving the steady-state PMD value with given divergence and threshold. Similar results can be derived for x_v .

Monitor characterization

The covariance matrix is bounded based on empirical data shown as follows. A 24-h data set was used collected on November 18, 2014, by Thales Electronic Systems at Pattonville, Germany using a GBAS Multipath Limiting Antenna (MLA) BAE-ARL1900 and Septentrio PolRx4 receiver. The elevation mask is 5° , the time constant is 30 s and the ground steady state is 360 s after initialization

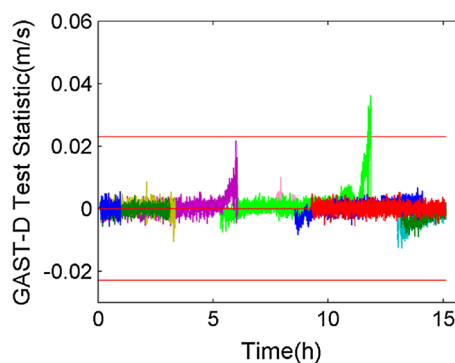


Fig. 5 GAST-D CCD monitor

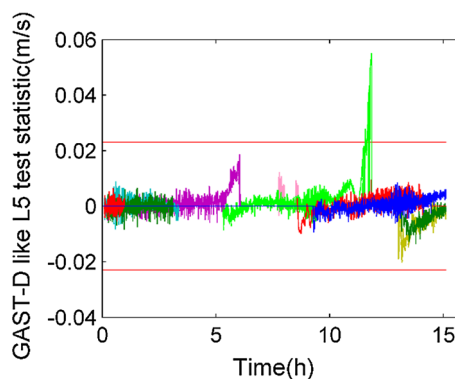


Fig. 6 GAST-D like L5 CCD monitor

(DO-253C 2008). There were in total 8 GPS satellites visible with both L1 and L5 measurements available (SV1, 3, 6, 9, 24, 25, 17 and 30). The phase measurements are checked against cycle slips for all statistics (Gao and Li 1999). The GAST-D CCD test metric and GAST-D like L5 test metric are shown in Figs. 5 and 6, where the latter one is designed as the GAST-D CCD monitor using L5 measurements instead of the L1.

With the threshold set as 0.023 m/s in GAST-D, there is a false alarm triggered in both Figs. 5 and 6 with SV27 due to ionospheric delay at low elevation angles resulting in an obliquity effect. This can be avoided with the proposed GAST-F test metrics with the ionosphere delay removed. The x_1, x_2, x_3, x_4 used in the GAST-F test metric are shown in Fig. 7 with the different colored time series relating to different satellites. The standard deviations of these statistics are shown in Table 2, and the correlation coefficients are listed in Table 3.

The gap in Fig. 7c, d is caused by limited L5 data to estimate the receiver clock in (21). This will be greatly reduced with the L5 full operational capability expected about 2024 for GPS.

The standard deviation ratio before and after filtering of the L1 code multipath dominated $\dot{\chi}_{C1}$ is $\sigma_{\dot{\chi}_{C1}}/\sigma_{x_1} = 124$. It has been observed that for $\dot{\chi}_{C2}$ and $\dot{\chi}_{C3}$ this ratio is not

Fig. 7 Four statistics used to form the Chi-squared GAST-F test metric **a** x_1 , **b** x_2 , **c** x_3 , **d** x_4

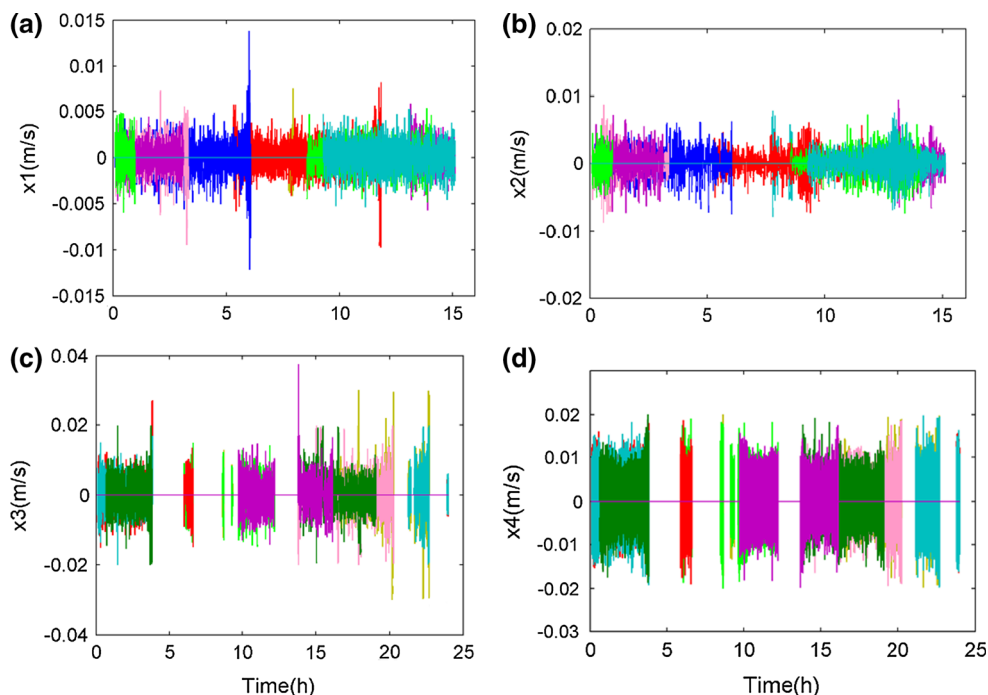


Table 2 Standard deviation before and after filtering

Before	$\dot{\lambda}_1$	$\dot{\lambda}_5$	$\dot{\lambda}_{C1}$	$\dot{\lambda}_{C2}$	$\dot{\lambda}_{C3}$	$\dot{\lambda}_{C4}$
m/s	0.145	0.0456	0.145	0.0458	0.358	0.00352
After	$F_m \dot{\lambda}_1$	$F_m \dot{\lambda}_5$	x_1	x_2	x_3	x_4
m/s	0.00320	0.00552	0.00117	0.00115	0.0051	–

Table 3 Covariance and correlation coefficient ρ

covariance, ρ	$\dot{\lambda}_{C1}$	$\dot{\lambda}_{C2}$	x_1
$\dot{\lambda}_{C2}$	1.2×10^{-5} , 0.0018		
$\dot{\lambda}_{C3}$	0.043, 0.84	–0.0025, –0.38	
x_4			-2.4×10^{-9} , –0.00058

consistent. This may explain the fact that a low-frequency antenna bias has been observed on L5 under the experimental setup employed. Improvement of the antenna tuning to L5 is to be expected for future testing and implementation that should eliminate this bias. In order to populate the covariance matrix, the standard deviation after filtering given in Table 2 is used for $\dot{\lambda}_{C1}$, while for $\dot{\lambda}_{C2}$ and $\dot{\lambda}_{C3}$ the standard deviations before filtering are used after application of the ratio derived for $\dot{\lambda}_{C1}$. The selected data are shown in red in Table 2. The covariance is derived in the same way. Therefore, the derived values are $\sigma_{x_2} = 0.00037$ m/s, $\sigma_{x_3} = 0.0029$ m/s, $cov(x_1, x_3) = 2.8 \times 10^{-6}$ (m/s)² and $cov(x_2, x_3) = -1.6 \times 10^{-7}$ (m/s)², while σ_{x_1} and σ_{x_4} are used directly from Table 2.

As shown in Table 3, the correlation coefficient of $\dot{\lambda}_{C1}$ and $\dot{\lambda}_{C2}$ is 1.8×10^{-3} , which is considered negligible. Using the same standard deviation ratio 124, the correlation coefficient of x_1 and x_2 after filtering should have the same value, which is also negligible. Since the correlation of x_1 and x_4 is negligible in Table 3, the correlation of x_2 and x_4 should be smaller and negligible too, which can be concluded from (15) and (18). Therefore, the two covariance matrices are,

$$Q_u = \begin{bmatrix} 0.0012^2 & 0 & 2.8 \times 10^{-6} \\ 0 & 0.00037^2 & -1.6 \times 10^{-7} \\ 2.8 \times 10^{-6} & -1.6 \times 10^{-7} & 0.0029^2 \end{bmatrix}$$

$$Q_v = \begin{bmatrix} 0.0012^2 & 0 & 0 \\ 0 & 0.00037^2 & 0 \\ 0 & 0 & 0.0033^2 \end{bmatrix}$$

The GAST-D monitor is able to detect if there is a difference of the code and carrier divergence on L1 d_1 . The performance of the proposed GAST-F nonlinear monitor varies with d . With the same divergence magnitude, some fault modes produce larger non-centrality parameters, making them easier to detect. Figure 8 shows the probability of missed detection performance at steady state for the GAST-D monitor, the GAST-D like L5 monitor and the GAST-F single-divergence fault modes (MC1, MC5, MP1 and MP5) with given covariance matrices.

The standard deviation of the test metric of the GAST-D like L5 monitor is set as 0.0071 m/s. It is bounded in the same way as in GAST-D (Simili and Pervan 2006) as a sum of the nominal ionospheric divergence

($0.00399 \times \gamma$) m/s which gives 0.0071 m/s and the filtered code noise. The latter may be regarded as negligible, since the L5 filtered code noise is smaller than L1 and the ionospheric divergence is larger. Therefore, the threshold is 0.0415 m/s, and the GAST-D like L5 monitor is able to detect any difference of the code and carrier divergence on L5.

It is shown in Fig. 8 that the GAST-D like L5 and GAST-D CCD monitors have worse performance than the proposed monitor since the metric standard deviations must be inflated for non-Gaussian ionospheric divergences. With the same PMD value, the GAST-F monitors detect a divergence less than half the size of the GAST-D one for code-only divergences. The two GAST-F monitors have similar performance with single divergences, where a divergence of 1–2 mm/s can be detected within a PMD of 10^{-9} . Since the other GAST-D monitors are able to detect carrier phase deviations at a similar level (Stakkeland et al. 2014), the advantage of the GAST-F monitor for carrier phase-only divergences is not significant. It should be noted that the performance level is demonstrated assuming the ratio before and after filtering is 124 for all data. So the result with MC1 in Fig. 8 is trustworthy, while the other fault modes need further data. Also, the detectable divergences cited here do not include ionospheric divergence. However, in the real environment, the influence of both the nominal ionospheric divergence on the single-frequency monitors and the residual ionospheric delay not removed on dual-frequency monitors should be considered at the level of mm/s.

The purpose of overbounding is to introduce a conservative model to be used in demonstrating the integrity compliance. To gain a conservative Chi-squared distribution, there are two parts to be considered (Rife 2012): (1) the bounding of the non-Gaussian tails of statistics and (2) the de-correlation and scaling of the statistics. Part 2 is not needed when overbounding Q_v , which is diagonal. To carry out 1, the statistics are first normalized with 10° elevation angle interval. The results of x_l versus elevation angle are

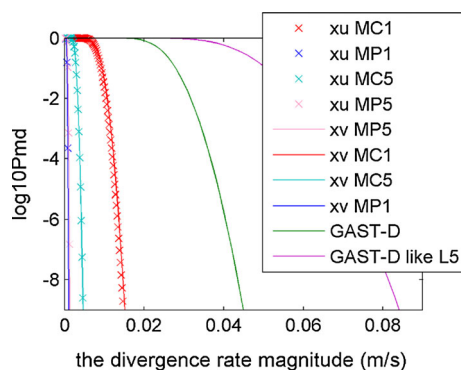


Fig. 8 CCD monitor performance at steady states

shown in Fig. 10. The cumulative distribution function (CDF) of the normalized statistics is then generated. To generate a conservative bound, a simple CDF bounding is used as shown in Fig. 10. The inflation factors of the standard deviation of x_1, x_2, x_3 and x_4 are 1.4, 1.4, 1.4 and 1.3.

As shown in Fig. 9, the results at low elevations are much worse. An alternative approach is to estimate the standard deviation separately for elevation angles lower than 30° , which could avoid excessive overbounding. The bounded Q_v is,

$$Q_v = \begin{bmatrix} 0.0017^2 & 0 & 0 \\ 0 & 0.00050^2 & 0 \\ 0 & 0 & 0.0046^2 \end{bmatrix}$$

The metric choice x_v is preferred over x_u for the following reasons: (1) x_u and x_v have very similar performance as shown in Fig. 8; (2) Q_v is a diagonal matrix with negligible correlation, which greatly simplifies the process of overbounding a Chi-squared distribution (Rife 2012); and (3) x_4 is used without filtering, reducing the monitor’s response time to divergences on phase measurements.

Monitor compliance

GAST-D and consequently GAST-F requirements are derived on the basis of three specific airworthiness conditions relating to the autoland method, namely the nominal case, the limit case and the malfunction case (Murphy 2002; FAA 1999; EASA 2003). Aircraft touchdown performance must be assured in the limit and malfunction cases which consider the presence of a fault bias on the position assuming a projection factor of less than 4 from position domain to range domain, potentially as a result of a satellite payload fault (SARPs 2009). Consideration of these two cases led to the derivation of a PMD curve for the differential range error E_R shown in Fig. 11, where the blue line is the requirement and the green line is an example Gaussian monitor satisfying the requirement.

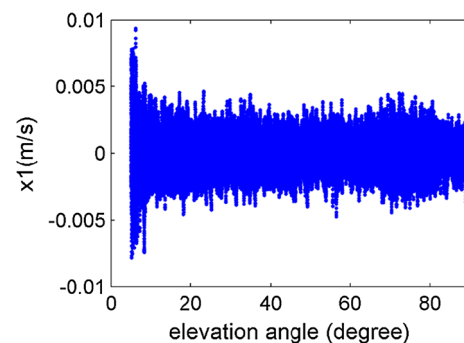


Fig. 9 x_1 vs elevation angle

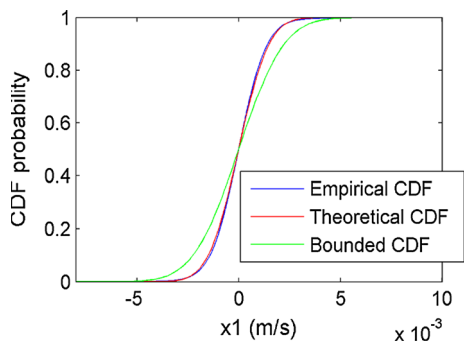


Fig. 10 Bounding the CDF of x_1

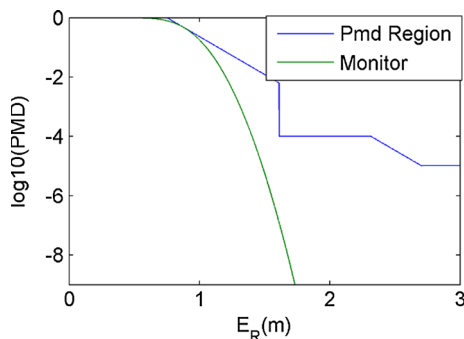


Fig. 11 GAST-D PMD compliance requirement

A mapping function f is defined as the projection from E_R to the non-centrality parameter δ . The mapping is only linear when all filters are in steady state which is not in general the case. The PMD may then be expressed as a function of δ ,

$$P_{md}\{E_R(t_A)\} = P_{md}\{f^{-1}[\delta(t_A + TTDBA - \tau_G)]\} \quad (31)$$

where TTDBA (Time To Detect And Broadcast) is the time between the magnitude of the differential error exceeding E_R and the last bit of the integrity data leaving the VDB. In GAST-D, the required time to alert is 2.5 s from the time at which the fault becomes hazardous. The required value of TTDBA is chosen as 1.5 s to allow a 1-s margin of delays and missed messages. The ground latency τ_G is the time difference between the formation of the test metric and the last bit of integrity data leaving the VDB.

The simulation setup is outlined in Table 1, and the results followed for the considered GAST-F processing modes (SF1, SF5, DF1, DF5, IF) are compared with the GAST-D compliance curve. Some previous demonstrations have considered the steady-state performance with a linear mapping function. In order to fully protect the user, the simulations undertaken here have considered the full threat space and the transient phase of the fault. To check compliance with the PMD requirements, both the PMD and E_R must then be determined at all points in this threat space.

Table 4 Simulation configuration over the threat space

	GAST-D	GAST-F
τ_m	30 s	
τ	30 s	100 s
t_f	460 s	
$t_{g,0}$	0 s	
t_{delay}	50 s	
τ_G	1.5 s	3 s
f_C	2 Hz	0.5 Hz
t	[0:1:1800] s	
$t_{a,0}$	[300:3:600] s	[400:4:1400] s
d	[0:0.0002:0.05] m/s	[0:0.0001:0.025] m/s code [0:0.00002:0.005] m/s phase

First, the behavior of E_R is analyzed with the condition that the generated PMD is $>10^{-9}$. Based on the analysis of the behavior of data filters and monitors with regards to the CCD fault, the configuration is chosen in Table 4 to cover the worst case where t is the simulation duration, f_C is the correction update rate, [] is used to denote the parameter range (1st and 3rd) and resolution (2nd) tested. For example, [0:1:1800] s means the value t is tested from zero to 1800 s with each epoch adding 1 s. A slower update rate of the correction 0.5 Hz is used in the simulation for GAST-F to accommodate more VDB information considering the data processing modes for multiple-constellation and dual-frequency measurements.

In a full and correct demonstration of integrity monitoring compliance, all monitors are implemented. In this analysis, only the CCD monitor is presented without the aid of other monitors. To speed up the simulation, the non-central Chi-squared distribution is approximated by a central Chi-squared distribution or biased normal distribution where appropriate with sufficient accuracy (Johnson et al. 1970). Based on the analysis presented above, the worst-case situation is summarized as follows:

- (a) Larger E_R results from situations where the ground station smoothing filter is converged and broadcasting and the airborne user acquires the satellite around the fault onset time.
- (b) Larger E_R results from the variant time constant airborne filter (as opposed to the invariant one). Therefore, only the variant cases need to be demonstrated to satisfy the requirement.
- (c) GAST-D E_R and CCD test metric depend only on the difference in code and carrier phase divergence magnitudes $d_1 = d_{\rho 1} - d_{\phi 1}$, not their individual magnitudes, and therefore, only one fault mode is needed for the GAST-D compliance analysis.

The following figures plot the PMD and E_R pairs following an exhaustive search of the parameter ranges expressed in Table 3. Figure 12 is a collection of PMD and E_R values in the threat space presenting the GAST-D monitor performance. Compliance of the GAST-D CCD monitor to the requirement is therefore established. Similarly, Fig. 13 shows the GAST-D like L5 results which are not compliant.

Figure 14 shows the monitor performance for the GAST-F x_v monitor with the DF1 processing technique for the fault modes MC1, MP1 and MP5. GAST-F x_v monitor with the IF processing method is shown in Fig. 15 for MC1, MP1, MC5 and MP5.

It is observed in Fig. 14 that under the processing DF1 is able to satisfy the requirement with single-divergence fault modes. With DF5 MC5, better performance is expected than with DF1 MC1 using the more precise L5 measurements in both data processing and CCD monitor. Therefore, for an airborne user utilizing DF5 processing, the PMD compliance with single-divergence fault modes can also be concluded. IF MC1 is the most critical case within the single-divergence fault modes in Fig. 15, mainly due to the 2.26 inflation factor in the IF data processing method. The carrier rate monitor and excessive acceleration monitors (Brenner and Liu 2010) are unable to help protect against the purely code-based divergences.

The full-divergence modes including MC1P15 for DF1 and MC15P15 for IF are shown in Fig. 16. The divergence loops are set as $[-0.025:0.0025:0.025]$ m/s on code and $[-0.005:0.0005:0.005]$ m/s on phase, and the resolution of the t_a loop is 10 s to cover the worst case with a tolerable simulation time.

In order to enable compliance with the existing GAST-D requirements, one solution could be to lengthen t_{delay} , the delay to introducing a ranging measurements into the position solution. It was observed that in order to meet the GAST-D requirements, the delay of incorporating a satellite’s measurements, t_{delay} , needs to be extended from the 50 s in GAST-D to 132 s for IF users in GAST-F, which is shown in Fig. 17.

It may be that the GAST-F PMD requirement curve can be relaxed on account of the improved geometry available from

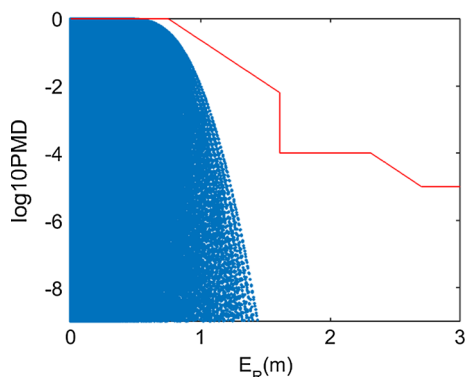


Fig. 12 Simulated results of GAST-D

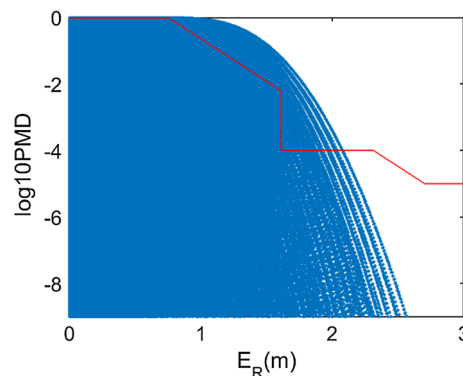


Fig. 13 Simulated results of GAST-D like L5

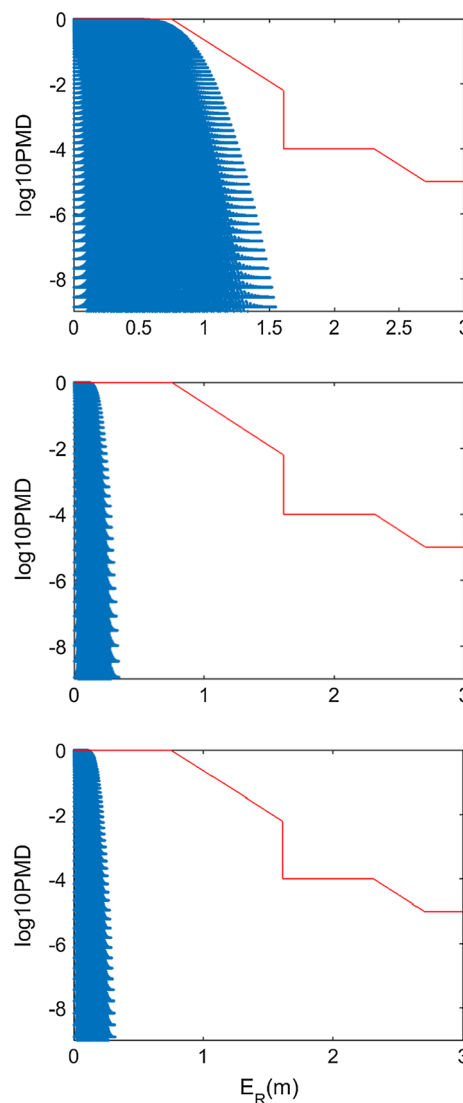


Fig. 14 Simulated results of GAST-F DF1 with single-divergence modes: (top) MC1, (middle), MP1, (bottom) MP5

multiple constellations. Even with the GAST-D PMD requirement, the better geometry from multiple constellations

Fig. 15 Simulated results of GAST-F IF with single-divergence modes: **a** MC1, **b** MC5, **c** MP1, **d** MP5

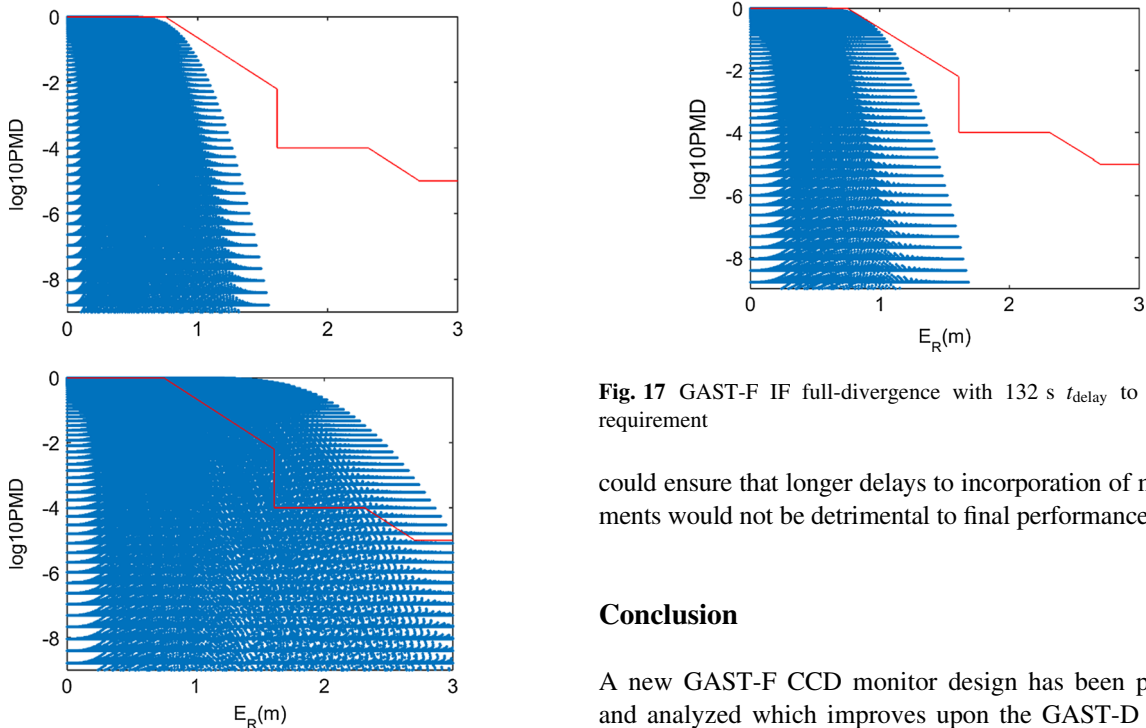
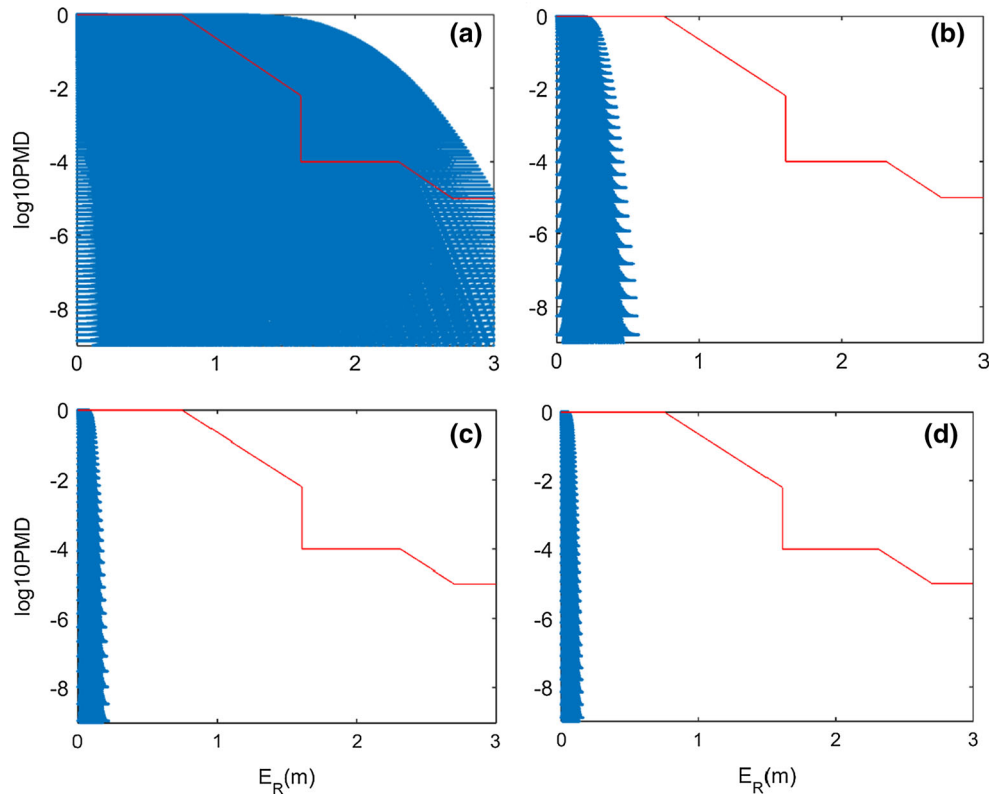


Fig. 16 Simulated results of GAST-F with full-divergence modes: (top) DF1, (bottom) IF

Fig. 17 GAST-F IF full-divergence with 132 s t_{delay} to meet the requirement

could ensure that longer delays to incorporation of measurements would not be detrimental to final performance.

Conclusion

A new GAST-F CCD monitor design has been proposed and analyzed which improves upon the GAST-D monitor by removing the ionospheric divergence. It has been demonstrated that for aircraft employing IF smoothing techniques either under nominal mode or as a potential

backup, the maximum differential error is significantly inflated. Therefore, all such GAST-F CCD monitor designs would suffer from this handicap, especially when there is divergence on Code L1. The design proposed combats this by reducing the standard deviation of the metric by restricting it to the local multipath and noise of the receivers and not to nominal ionospheric delays. This has the benefit of increasing the level of integrity protection for a given false alarm probability while also reducing conservatism in overbounding.

Acknowledgments This work is funded by SESAR Joint Undertaking within the frame of the Single European Sky ATM Research (SESAR) Program. The authors would like to thank Thales Electronic Systems for the use of collected data under the SESAR Program.

References

- Brenner M, Liu F (2010) Ranging source fault detection performance for category III GBAS. In: Proceedings of ION GNSS 2010, Institute of Navigation, Portland, 21–24 Sept, pp 2618–2632
- DO-229D (2006) Minimum operational performance standards for global positioning system/wide area augmentation system airborne equipment, RTC
- DO-253C (2008) Minimum operational performance standards for GPS local area augmentation system airborne equipment, RTCA
- EASA (2003) CS-AWO, joint aviation requirements—all weather operations, Subpart 1, Automatic Landing Systems
- ED-114A (2013) Minimum operational performance specification for global navigation satellite ground based augmentation system ground equipment to support category I operations, EUROCAE
- FAA (1999) Advisory circular 120-28D, criteria for approval of category III weather minima for takeoff, landing and rollout. FAA, Washington
- Gao Y, Li Z (1999) Cycle slip detection and ambiguity resolution algorithms for dual-frequency GPS data processing. *Mar Geod* 22(3):169–181
- Gleason S, Gebre-Egziabher D (2009) GNSS applications and methods, Artech House, ISBN 1-596-93329-1
- Hatch R (1982) The synergism of GPS code and carrier measurements. In: Proceedings of the third international symposium on satellite Doppler positioning at physical sciences laboratory of New Mexico State University, 8–12 Feb, vol. 2, pp 1213–1232
- Hwang PY, McGraw GA, Bader JR (1999) Enhanced differential GPS carrier-smoothed code processing using dual-frequency measurements. *Navigation* 46(2):127–138
- Johnson NL, Kotz S, Balakrishnan N (1970) Continuous univariate distributions, vol 2. Wiley, New York ISBN 0-471-58494-0
- Kay S (1998) Fundamentals of statistical signal processing, volume II: detection theory. Prentice Hall, Upper Saddle River
- Milner C, Guilbert A, Macabiau C (2015) Evolution of corrections processing for the MC/MF ground based augmentation system (GBAS). In: Proceedings of ION ITM 2015, Institute of Navigation, Dana Point, California, 26–28 Jan, pp 364–373
- Murphy T (2002) Development of signal in space performance requirements for GBAS to support CAT II/III landing operations. In: Proceedings of ION GPS 2002, Institute of Navigation, Portland, 24–27 Sept, pp 20–28
- Rife J (2012) Overbounding missed-detection probability for a Chi square monitor. In: Proceedings of ION GNSS 2012, Institute of navigation, Nashville, 17–21 Sept, pp 1348–1368
- SARPs (2009) GBAS CAT II/III development baseline SARPs, ICAO NSP. http://www.icao.int/safety/airnavigation/documents/gnss_cat_ii_iii.pdf
- Simili DV, Pervan B (2006) Code-carrier divergence monitoring for the GPS local area augmentation system. In: Proceedings of PLANS, IEEE/ION position, location, and navigation symposium, San Diego, 25–27 Apr, pp 483–493
- Stakkeland M, Andalsvik Y, Jacobsen K (2014) Estimating satellite excessive acceleration in the presence of phase scintillations. In: Proceedings of ION GNSS 2014, Institute of Navigation, Tampa, 8–12 Sept, pp 3532–3541
- Tang H, Pullen S, Enge P, Gratton L, Pervan B, Brenner M, Scheitlin J, Kline P (2010) Ephemeris type A fault analysis and mitigation for LAAS. In: Proceedings of PLANS, IEEE/ION position, location, and navigation symposium, Indian Wells, 4–6 May, pp 654–666



Yiping Jiang is currently a postdoctoral fellow within the Telecom Lab at ENAC. She obtained her Ph.D. degree from the School of Surveying and Geospatial Engineering in University of New South Wales in 2014. Her main research topics include precise positioning and integrity monitoring technologies. Currently, she is working on A-RAIM and GBAS with multi-constellation multi-frequency.



Dr. Carl Milner is an assistant professor within the Telecom Lab at the Ecole Nationale de l'Aviation Civile, Toulouse France. He currently lectures on many aspects of navigation science and technology including radio navigation aids, signal processing, positioning algorithms and GNSS for civil aviation. His research work addresses the design of integrity monitoring algorithms for current GNSS signals and the future multi-constellation multi-frequency environment.



Christophe Macabiau graduated as an electronics engineer in 1992 from the ENAC in Toulouse, France. Since 1994, he has been working on the application of satellite navigation techniques to civil aviation. He received his Ph.D. in 1997 and has been in charge of the signal processing laboratory of ENAC since 2000. He is now the head of the Telecom Lab at ENAC.